Ohshimo et al. *EPJ Techniques and Instrumentation* (2023) 10:11
https://doi.org/10.1140/epjti/s40485-023-00098-1
EPJ.org
EPJ Techniques and Instrumentation
RESEARCH ARTICLE
Open Access

Cryogenic ion mobility-mass spectrometry for the study of conformations of host-guest complexes

Keijiro Ohshimo[1*], Xi He[1], Ryosuke Ito[1], Kengo Tsunoda[1], Sota Tainaka[1] and Fuminori Misaizu[1*]

*Correspondence:
ohshimo@tohoku.ac.jp;
misaizu@tohoku.ac.jp
[1]Department of Chemistry, Graduate School of Science, Tohoku University, Sendai 980-8578, Japan

Abstract

Variable-temperature cryogenic ion mobility-mass spectrometry (VT-Cryo-IM-MS) was developed to examine the conformations of host-guest complexes. The VT-Cryo-IM-MS consists of an electrospray ionization source, a quadrupole ion trap, a cryogenic ion drift tube, and a time-of-flight mass spectrometer. The ion drift tube was cooled to 83 K with liquid nitrogen. Two sets of ion funnels are installed at the source and the drift tube to focus the ion beam. We used Li^+-encapsulated fullerene ($Li^+@C_{60}$) as a reference ion to examine the ion-mobility resolution of the VT-Cryo-IM-MS apparatus because this ion has a rigid structure with a single conformer. The temperature dependence of collision cross section (CCS) of $Li^+@C_{60}$ and the resolution of the apparatus were determined at each temperature. We examined the conformations of host-guest complexes of a series of metal ions (M = Ca^{2+}, Na^+, Ag^+, K^+, Rb^+, and Cs^+) with dibenzo-24-crown-8 (DB24C8) by Cryo-IM-MS. All CCS distributions were fitted with two Gaussian functions which are assigned to closed and open conformers. These closed and open conformers have different distances between the two benzene rings of DB24C8. The abundance ratio of closed conformers for these M(DB24C8) complex ions depends on the guest M ion with an order, $Ca^{2+} < Na^+ < Ag^+ < Cs^+ < Rb^+ < K^+$. The stability of the closed conformer of K^+(DB24C8) originates from the benzene ring positional relationship which is quite close to that of the free benzene dimer. This special benzene dimer-like conformation produces the strong π-π interaction between the benzene rings of K^+(DB24C8).

Keywords: Ion mobility-mass spectrometry; Host–guest complex; Crown ether; Isomer separation; Conformation

1 Introduction

Supramolecules are formed by assembling multiple molecules through intermolecular interactions and exhibit advanced functions that cannot be realized by a single molecule. Structures of supramolecules can be revealed by X-ray crystal structure analysis when the single crystal is obtained. Recently, gas-phase laser photodissociation spectroscopy was actively performed to study structures of supramolecular ions [1]. In this technique, a supramolecular ion in solution is isolated in the gas phase by electrospray ionization. Especially in cryogenic laser spectroscopy, the vibrational temperature of the isolated ion

is decreased to ∼10 K by using the cryogenic ion trap. This cryogenic technique enables us to observe vibrationally resolved sharp absorption spectra of supramolecules. However, more than one conformer often coexists in the gas phase because the structures of supramolecular ions are flexible. In this case, a complicated spectrum is observed since the spectral bands of each conformer may overlap. A complicated spectrum prevents the determination of structures and abundance ratio of conformers. The functions of the supramolecules are closely related to conformations. Therefore, to elucidate the origin of the functions it is important to separate and determine the geometrical structures of conformers. Ion mobility-mass spectrometry (IM-MS) is known as a powerful technique to separate conformers in the gas phase [2–4]. Size- and conformer-selected absorption spectra of supramolecular ions can be obtained by the coupling of IM-MS with photodissociation spectroscopy [5–7].

A host-guest complex is a simple molecule of flexible supramolecule. IM-MS has been used to study conformers of host-guest complexes in the gas phase at room temperature [3, 8, 9]. In IM-MS, we measured the time distribution of the ions to pass through the drift tube (several milliseconds) and determined collision cross sections (CCSs) between the ions with a buffer gas. Conformations of complex ions can be determined from the comparison between experimental and theoretical CCSs of the ions. However, at room temperature, the structure of a host-guest complex fluctuates among several conformers with the use of thermal energy. Cryogenic IM-MS has also been performed using a drift tube cooled by liquid nitrogen [10–25]. In some cases, the kinetics of isomerization of ions can be studied by variable-temperature cryogenic IM-MS (VT-Cryo-IM-MS) [15–17, 19, 20, 24, 26, 27]. Because VT-Cryo-IM-MS is performed in the gas phase, the essence of the structural change of ions can be elucidated without the influence of the solvent molecules. Furthermore, as the isomerization rate decreases at low temperatures, it is possible to elucidate the mechanism of the fast conformational exchange kinetics that are difficult to study in the liquid phase at room temperature.

In this paper, we present recent developments in the conformation analysis of host-guest complexes using our VT-Cryo-IM-MS spectrometer. We examined the information on (1) what kinds of conformations exist, (2) how stable each conformation is energetically, and (3) how high the activation energy barrier is between the conformations. We developed VT-Cryo-IM-MS which can freeze supramolecular structures and separate conformers in the gas phase. Furthermore, we studied the kinetics and dynamics of conformational changes by VT-Cryo-IM-MS analysis combined with theoretical calculations of isomerization pathways [24].

Section 2 of this paper describes the details of our VT-Cryo-IM-MS apparatus. In Sect. 3, we discuss the resolving power of ion mobility in VT-Cryo-IM-MS which is necessary to analyze the isomerization kinetics from IM-MS data. Finally, we show the results of separation and isomerization analysis of conformers of dibenzo-crown-ether complexes with metal ions which are known as fundamental host-guest complexes.

2 Design of the apparatus

2.1 Vacuum system

Details of the experimental apparatus were given elsewhere [25]. The VT-Cryo-IM-MS apparatus developed in the present study is shown in Fig. 1. The vacuum apparatus consists of four chambers (1)–(4), which are separated by conductance-limiting apertures.

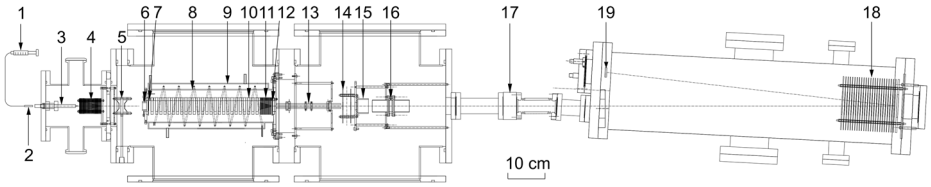

Figure 1 Schematic diagram of the cryogenic IM-MS apparatus. (1) Syringe pump, (2) metal capillary, (3) heated desolvation capillary, (4) ion funnel, (5) quadrupole ion trap, (6) ion lens, (7) entrance aperture of a drift tube, (8) ion drift tube, (9) liquid nitrogen jacket, (10) electrodes for ion-drifting, (11) ion funnel, (12) exit aperture of the drift tube, (13) octopole ion guide, (14) acceleration electrodes of TOF-MS, (15) ion-beam deflector, (16) einzel lens, (17) gate valve, (18) TOF-MS reflectron electrodes, and (19) dual microchannel plate ion detector

Table 1 The vacuum pressure during measurement, pumping speed, and components in each chamber[a]

Chambers	Pressure / Pa	Pumping speed / L s^{-1}	Components
1	25	86	ESI ion source
2	2.0×10^{-2}	2000	QIT and drift tube
3	1.4×10^{-3}	2000	Ion guide and acceleration electrodes
4	1.3×10^{-4}	500	Reflectron electrodes and detector

[a]The pressure and temperature of the He buffer gas inside the drift tube are 0.60 Torr and 85 K, respectively.

The following components were placed in each chamber of (1) to (4): (1) electrospray ionization (ESI) ion source with ion funnel electrodes, (2) quadrupole ion trap (QIT) and cryogenic ion drift tube with an ion funnel, (3) octopole ion guide and acceleration electrodes of a time-of-flight mass spectrometer (TOF-MS), and (4) reflection electrodes of a reflectron-type TOF-MS, and a microchannel plate for ion detection. The vacuum pressure during measurement and pumping speed in each chamber are summarized in Table 1.

2.2 Ion source

A home-made electrospray unit was used for the ion source. Inorganic salt ($CaCl_2$, NaCl, $AgNO_3$, KCl, RbCl, or CsCl) and dibenzo-24-crown-8 (DB24C8) were dissolved in methanol to prepare the solution with a concentration of 0.1 mM. The solution was delivered to a metal capillary (Hamilton, 22033-01, capillary o.d. = 0.21 mm, i.d. = 0.108 mm) at 2.0 μl/min by a syringe pump (Harvard, Model 11 Elite). The exit of the capillary was positioned at ∼4 mm upstream from the entrance of a heated desolvation capillary (Thermo Fisher, 97000-98002, capillary i.d. = 0.4 mm), which was attached at the inlet end of the vacuum chamber (1). The temperature of the desolvation capillary was maintained at ∼350 K. High voltage (+2.8 kV) was applied between the metal capillary and the desolvation capillary to make electrospray. The desolvation capillary was floated at a voltage of +350 V from the ground. The exit of the desolvation capillary was in the first vacuum chamber pumped by a mechanical booster pump (Edwards, EH250) and a rotary pump (Edwards, E2M40). The entrance of an ion funnel was positioned close to the end of the desolvation capillary. The design of the ion funnel was based on the paper by Smith and coworkers [28]. The ion funnel consists of 29 stainless-steel electrodes (1 mm thick) which are separated by 1 mm thick PTFE washers and electrically connected by 500 kΩ resistors. The aperture diameters of the electrodes decrease linearly from 29 mm to 1 mm. DC voltages were applied to the first and the last electrodes of the ion funnel to make the static

electric field (17.5 V/cm) to guide the ions downstream. In addition to the DC, opposite phases of radio frequency (RF) voltages were applied to alternating electrodes of the funnel to confine the ions radially. The RF voltage ($V_{p\text{-}p}$ = 100 V, 800 kHz) for the funnel was generated by the power supply based on the design of Jones and Anderson [29]. The first chamber was separated from the next chamber with the last electrode of the ion funnel.

After passing through the ion funnel, ions were introduced to the QIT (Jordan TOF Products, C-1251) in the second chamber. Ions were typically accumulated for 40 ms in the QIT by a RF electric field ($V_{p\text{-}p}$ = 700 V, 1 MHz) generated by the power supply (Jordan TOF Products, D-1203). Helium gas was introduced to the QIT with 16 sccm for efficient ion-trapping. After accumulation in the QIT, ions were next injected into the cryogenic ion drift tube by a pulsed electric field with a kinetic energy of 30 eV in the laboratory frame at a given time ($t = t_0$). The repetition rate of the ion injection was 20 Hz.

2.3 Cryogenic ion drift tube

The cross-sectional view of the cryogenic ion drift tube is shown in Fig. 2. The ion drift tube consists of a stainless-steel tube (84 mm i.d.), which was mounted in a vacuum chamber with a PTFE plate in between for thermal insulation. The total drift length from the entrance to the exit apertures of the drift tube was 327 mm. The hole diameters of these entrance and exit molybdenum apertures were 1.5 mm and 2.0 mm, respectively. The thicknesses of the apertures were both 0.5 mm. Stacked ring electrodes were placed in the drift tube, followed by the ion funnel to collect the ions. The 26 aluminum ring electrodes (44 mm o.d., 28 mm i.d., 6 mm thick) were electrically connected by 1 MΩ resistors. The spacing between adjacent rings was fixed to 5 mm by inserting ceramic insulators between them. A static electric field of E = 6.1 V/cm was applied to the rings for ion drifting. The ion funnel consists of 16 stainless-steel electrodes (1 mm thick) which were separated by PTFE washers of the same thickness. The aperture diameters of the electrodes decrease linearly from 18 mm to 3 mm. The gradient of the static electric field (E = 6.1 V/cm) was

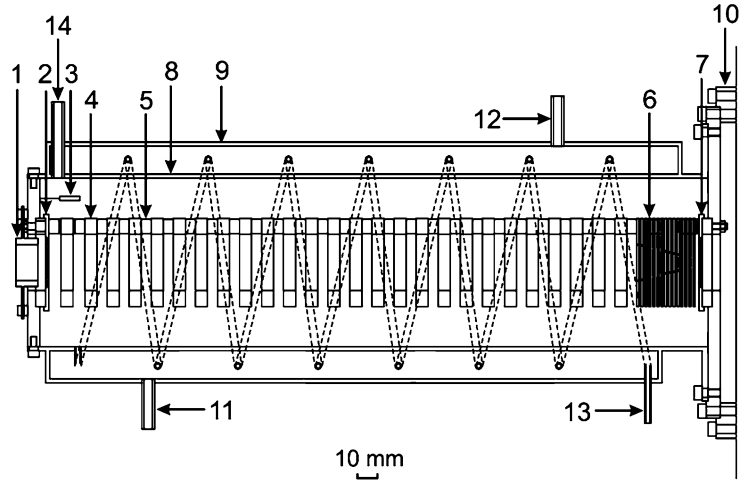

Figure 2 The cross-sectional view of the cryogenic ion drift tube. (1) ion lens, (2) entrance aperture of the drift tube, (3) resistance temperature detector, (4) electrodes for ion drifting, (5) ceramic insulator, (6) ion funnel, (7) exit aperture of the drift tube, (8) drift tube housing, (9) liquid nitrogen jacket, (10) PTFE plate, (11) inlet of liquid nitrogen, (12) exit of liquid nitrogen, (13) 1/8-inch stainless-steel tubing for introducing He buffer gas, (14) 1/4-inch tubing for connection with a capacitance manometer

set to the funnel electrodes which was the same with the ion-drifting region. The RF voltage for the funnel was $V_{p\text{-}p}$ = 100 V with 1 MHz.

Liquid nitrogen was introduced and filled in a cryogenic jacket surrounding the ion drift tube. This design of the cryogenic jacket is similar to that reported by May and Russell [15]. The 1/8-inch stainless-steel tubing for He buffer gas was spirally wound and attached inside the cryogenic jacket. After cooling by liquid nitrogen, He buffer gas was introduced into the ion drift tube. In the present experiments, the temperature of He buffer gas was measured by a resistance temperature detector (OMEGA, 1PT100KN815) inserted into the drift tube from the entrance side. The flow rate of the He buffer gas was maintained at 174 sccm using a mass flow controller (HORIBA STEC, SEC-N100). At 83 K the pressure of He buffer gas was 0.600 Torr, which was measured by a capacitance manometer (Setra, Model 730). The E/N value was 8.8 Td under the above condition at 83 K (N is the number density of the buffer gas, 1 Td = 10^{-17} V cm^2). The buffer gas was leaked to the second and third chambers from the entrance and exit apertures of the drift tube. These chambers were separately pumped by diffusion pumps (Edwards, Diffstak 250/2000M).

2.4 TOF-MS and analysis method

After passing through the cryogenic ion drift tube, the ions were transported by the octopole ion guide to the acceleration region of the TOF-MS. The ions were accelerated to ~4 keV by pulsed electric fields between the acceleration electrodes at a given time later from the pulse for the injection into the drift tube, $t = t_0 + \Delta t$. The ions were introduced to the reflectron TOF-MS (Jordan TOF Products, D-850). This delay time between the two pulses, Δt, was defined as "arrival time", and was determined by digital delay/pulse generators (Stanford Research Systems, DG645) which were processed with LabVIEW program of a PC. The timing sequence is summarized in Fig. 3.

The flight time of an ion that is accelerated at a given arrival time consists of TOFs in three regions: (i) between the center of the QIT and the entrance of the drift tube, (ii) inside

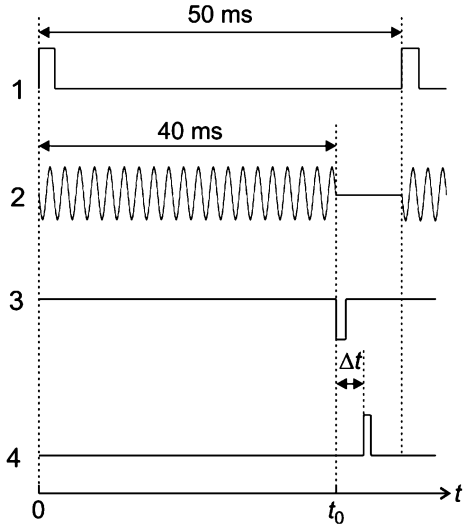

Figure 3 Experimental timing sequence. (1) Starting pulse of an experimental cycle (repetition rate = 20 Hz), (2) ion trapping period of the QIT (RF on, 40 ms), and ion unloading period (RF off), (3) unloading pulse for the QIT exit end cap, (4) ion acceleration pulse for TOF-MS (Δt, delay relative to unloading pulse of the ion trap). We defined Δt as the arrival time

of the drift tube, (iii) between the exit of the drift tube and the acceleration electrode of TOF-MS. Therefore, the arrival time consists of the drift time in the drift tube (t_d, region ii) and the time that the ion spends outside the drift tube (regions i and iii). The times in regions i and iii were calculated from the mass of the ion and various electrical potentials. The drift velocity of the ions in the drift tube, v_d, was calculated numerically to satisfy the measured arrival time. We obtained the time that an ion spends in the drift tube, t_d, from the measured arrival time. For example, in the Cryo-IM-MS of $Li^+@C_{60}$, typical times that the ion spends in regions i, ii, and iii were 0.030 ms, 2.369 ms, and 0.125 ms, respectively. The drift velocity v_d and the time t_d depend on the CCS between the ion and a He atom as noted below. Therefore, ions with different CCSs reach the acceleration region of the TOF-MS at different arrival times. Finally, the ions were mass-analyzed by the reflectron TOF-MS.

In the IM-MS measurement, we obtained a series of TOF mass spectra sequentially by scanning the arrival time. As a result, ions with different CCSs were separately detected at different arrival times in a two-dimensional plot of TOF versus arrival time. We obtained a plot of arrival time distribution (ATD), in which the total ion intensity of a certain TOF peak was shown as a function of the arrival time.

It is known that v_d is proportional to E, and the proportional constant (K) is called as ion mobility [30, 31]. The mobility K depends on the number density of the buffer gas N. To compare the mobility under different experimental conditions, the reduced mobility K_0 is defined as $K_0 = K \cdot (N/N_0)$, where N_0 is the Loschmidt's number. From the Mason-Schamp equation, the reduced mobility K_0 in the drift tube was given as:

$$K_0 = \frac{3q}{16N_0}\left(\frac{2\pi}{k_B \mu T_{eff}}\right)^{\frac{1}{2}} \frac{1}{\Omega}, \tag{1}$$

where q is the charge of the ion, k_B is the Boltzmann constant, μ is the reduced mass of the ion and the buffer gas atom, T_{eff} is the effective temperature of the ions, and Ω is a CCS [30, 31]. The effective temperature is given by $T_{eff} = T_{BG} + m_B v_d^2/k_B$, where T_{BG} is the buffer gas temperature and m_B is the mass of buffer gas. Therefore, the CCS of the ion is calculated from the measured arrival time of the ion, Δt.

3 Results and discussion

3.1 CCS and resolving power of ion mobility in VT-Cryo-IM-MS

In IM-MS, buckminsterfullerene monocation, C_{60}^+, is commonly used as a reference compound, which can be formed by a MALDI source [31]. However, this ion is unfortunately not suitable for efficient production, particularly in common ESI sources. In the present IM-MS experiments, we used Li^+-encapsulated fullerene ($Li^+@C_{60}$) [32, 33] as a reference compound to determine the resolving power of the ion-mobility apparatus because $Li^+@C_{60}$ is a structurally rigid ion composed of a single conformer. This ion can be efficiently introduced to vacuum by ESI with a solution of $[Li^+@C_{60}]TFSI^-$ salt ($TFSI^- = N(SO_2CF_3)_2^-$) in dichloromethane solvent [34]. This salt was synthesized by the anion exchange reaction of $[Li^+@C_{60}]PF_6^-$ salt (purchased from Idea International Co.) and has a high solubility in dichloromethane. Figure 4 shows the ATD of $Li^+@C_{60}$ measured under the present typical experimental condition (potential difference of the ion drift tube V = 200.0 V, temperature of He buffer gas T_{BG} = 83.11 K). In this experimental

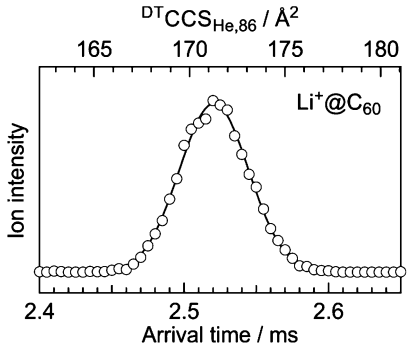

Figure 4 ATD of $Li^+@C_{60}$ ions. Pressure and temperature of He buffer gas in the ion drift tube were 0.6004 ± 0.0005 Torr and 83.11 ± 0.02 K, respectively. The curve is a Gaussian function for fitting the experimental plots (circles). $^{DT}CCS_{He,86}$ denotes the CCS between the ion and a He atom at T_{eff} = 86 K measured with the ion drift tube

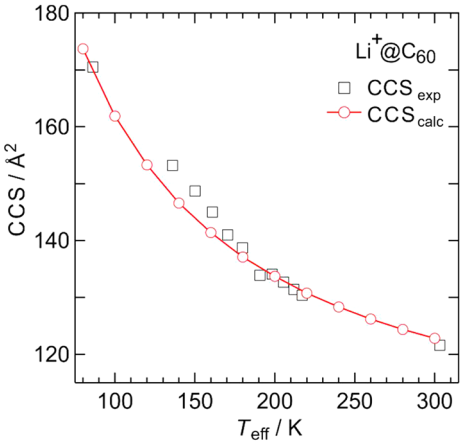

Figure 5 Temperature dependence of CCS of $Li^+@C_{60}$ with He buffer gas at 80–300 K which was obtained by our measurements and calculations

condition, the effective temperature is T_{eff} = 86.17 K. The ATD was fitted with a Gaussian function, and the experimental CCS at 86 K ($^{DT}CCS_{He,86}$) of $Li^+@C_{60}$ was determined to be 170.5 ± 0.2 Å^2 from the Gaussian peak. The error was estimated from the six independent measurements. This experimental CCS is almost equal to the theoretical CCS of $Li^+@C_{60}$ at T_{eff} = 86.17 K, 169.6 ± 1.0 Å^2, which was calculated by the trajectory method in the MOBCAL program [35]. In this calculation, we used the optimized structure of $Li^+@C_{60}$ calculated at the M06-2X/6-31+G(d) level with Gaussian 16 program [36].

As shown in the previous studies, the CCS of C_{60}^+ with He buffer gas increases with decreasing T_{eff} below 300 K (122.6 Å^2 at 300 K [37] to 180 Å^2 at 80 K [18]). Figure 5 shows the temperature dependence of CCS of $Li^+@C_{60}$ with He buffer gas at 80-300 K which was obtained by our measurements and calculations. Experimental CCS of $Li^+@C_{60}$ increases with decreasing T_{eff} (121.6 Å^2 at 303 K to 170.5 Å^2 at 86 K) as same as C_{60}^+. Theoretical CCSs of $Li^+@C_{60}$ reproduce experimental CCSs quantitatively. At lower temperatures, the amount of change in CCS with respect to temperature change is greater. As shown in Fig. 5, the theoretical CCS changes with 0.08 Å^2/K at T_{eff} = 300 K. On the other hand, CCS changes with 0.59 Å^2/K at T_{eff} = 80 K. Therefore, it is important to measure precisely and keep constant the temperature of He buffer gas to obtain the accurate experimental CCSs by Cryo-IM-MS.

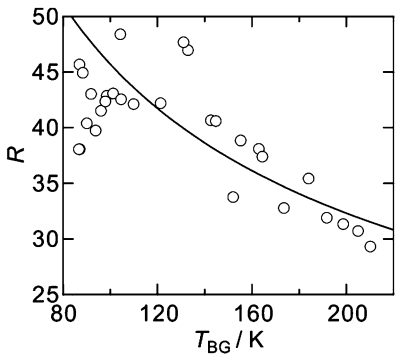

Figure 6 Temperature dependence of the resolving power R measured by the VT-Cryo-IM-MS of $Li^+@C_{60}$ ions at 83–210 K. Solid line is theoretical R calculated by using Eq. (2)

From the Gaussian function in the ATD of $Li^+@C_{60}$, the experimental resolving power of the ion mobility, R, of the apparatus at T_{BG} = 83 K was given by $R = t_d/t_w = 45.0 \pm 1.5$, where t_w is the full width at half maximum of the Gaussian function. In the drift-tube type IMS (DT-IMS), a pulsed ion packet is injected into the drift tube filled with the buffer gas. The ion packet is accelerated by the static electric field in the drift tube, and at the same time, it is decelerated by collisions with the buffer gas. During the acceleration and deceleration, the ion packet diffuses thermally in the drift tube. The resolution is lowered due to the diffusion because of the spatial broadening of the ion packet. The diffusion coefficient is known to be proportional to the temperature from the Einstein relation. Therefore, the resolving power is expected to be improved at cryogenic temperature because the diffusion becomes slower than that at room temperature. It is known that the R of DT-IMS is inversely proportional to the temperature of the buffer gas T_{BG} as shown in Eq. (2) [30].

$$R = \frac{1}{4}\sqrt{\frac{Vq}{k_B T_{BG} \ln 2}} \tag{2}$$

From this equation, the theoretical R of our apparatus was calculated to be R_{theo} = 50.2 (T_{BG} = 83 K, V = 200 V). Therefore, the experimental resolving power is 10% lower than the theoretical one. This decrease is probably caused by the spatial broadening of the ion packet at the entrance of the drift tube.

We measured the resolving power at each temperature between T_{BG} = 83–210 K. The T_{BG} was gradually raised by stopping the supply of liquid nitrogen after T_{BG} reached 83 K. The flow rate of He buffer gas was maintained at 174 sccm by using a mass flow controller. Figure 6 shows the temperature dependence of the resolving power R measured by VT-Cryo-IM-MS of $Li^+@C_{60}$. The R decreases with increasing T_{BG} and is nearly proportional to $T_{BG}^{-1/2}$, although the experimental error might have been large. This relationship between R and T_{BG} was used in the analysis of isomerization reactions of host-guest complexes by VT-Cryo-IM-MS [22].

3.2 Rapid isomerization reactions in host-guest complexes

We investigated the conformation of K^+ complexes with dibenzo-24-crown-8 (DB24C8) by IM-MS. Inokuchi and coworkers recently found the two different types of conformers of K^+(DB24C8) by ultraviolet photodissociation spectroscopy under cold (<10 K) gas-phase conditions [38]. The two types of conformers are closed and open conformers which have different distances between the two benzene rings of the crown ether. Figure 7a shows the

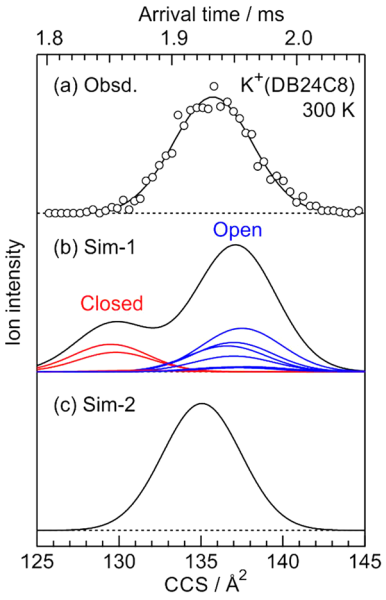

Figure 7 (**a**) The observed ATD of K^+(DB24C8) at 300 K (open circles) and a fitted Gaussian function (black curve). (**b**) The simulated ATD of K^+(DB24C8) by using relative abundances and CCSs of closed and open conformers at 300 K without isomerization. The ATD (black curve) is a sum of Gaussian functions (red and blue curves) whose areas depend on the abundances of the conformers. (**c**) The simulated ATD of K^+(DB24C8) with the averaged CCS (135.1 $Å^2$) for the expected conformers in the Boltzmann distribution at 300 K, under the assumption of the rapid isomerization reactions. The width of the ATD is determined from the mobility resolution of the apparatus at 300 K ($R = 24$)

ATD of K^+(DB24C8) obtained by IM-MS at room temperature. In this experiment, the temperature of the He buffer gas was 300 K, and its pressure was maintained at 1.10 Torr in the drift tube. The observed ATD (open circles) can be fitted with one Gaussian function (black curve), whose width coincides with the mobility resolution of the apparatus at 300 K (R = 24) determined from the IM-MS of $Li^+@C_{60}$. The CCS value was determined to be 135.7 $Å^2$ from the ATD peak of the fitted Gaussian function. To simulate the observed ATD, we calculated relative Gibbs energies and theoretical CCSs of the optimized conformers of K^+(DB24C8) at 300 K. In this calculation, a conformation search was performed by the CONFLEX 8 program with the MMFF94s force field [39, 40]. The conformers obtained by the search were further optimized using Gaussian 16 program [36] at the M05-2X/6-311++G(d,p) level. The vibrational analysis was also performed at the same level. The CCSs of the conformers with a He atom at 300 K were calculated by the trajectory method in the MOBCAL program [35].

The two different simulations of the observed ATD were performed under the assumptions that the isomerization rate between conformers in the drift tube is (1) much slower and (2) much faster than the drift time (∼2 ms). In the latter, multiple isomerization reactions were assumed to occur in the drift tube. In the simulation (1), relative abundances of the conformers were simply calculated from the Boltzmann distribution at 300 K based on the relative Gibbs energies, because the isomerization does not occur in the drift tube. Figure 7b shows the simulated ATD of K^+(DB24C8) under the assumption (1) by using relative abundances and CCSs at 300 K. The ATD (black curve) is a sum of Gaussian functions (red and blue curves) whose areas depend on the abundances of the closed and open conformers. As a result, a bimodal distribution was obtained which did not appear in the observed ATD.

On the other hand, we cannot distinguish conformers in the simulation (2) because the isomerization rapidly occurs in the drift tube. In this simulation, the ATD peak was observed at the arrival time weighted by the relative abundance of the conformers. Figure 7c shows the simulated ATD of K^+(DB24C8) with the averaged CCS (135.1 $Å^2$) for the ex-

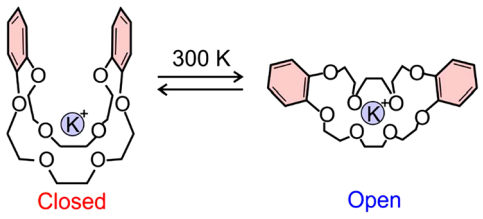

Figure 8 Isomerization reaction between closed and open conformers of K^+(DB24C8) at 300 K

pected conformers under the Boltzmann distribution at 300 K. The width of the ATD was determined from the experimental mobility resolution of the apparatus at 300 K (R = 24). The ATD in the simulation (2) well reproduces the observed ATD. Hence, the isomerization between the conformers occurs so rapidly in the drift tube at 300 K that the closed and open conformers of K^+(DB24C8) were not separately detected in IM-MS at room-temperature (Fig. 8).

3.3 Conformations of host-guest complexes

As described in Sect. 3.2, K^+(DB24C8) is a flexible host-guest complex that changes its structures by isomerization rapidly between conformers at 300 K (Fig. 8). To reveal the structural information of the complex, the rate of the isomerization needs to be slowed down under cryogenic conditions. We recently applied Cryo-IM-MS to M(DB24C8) (M = Na^+, K^+, and NH_4^+) in order to separate conformers [21–23]. In the present study, we extended the previous study to other metal guest ions as shown in Table 2. Figure 9 shows CCS distributions of the M(DB24C8) (M = Ca^{2+}, Na^+, Ag^+, K^+, Rb^+, Cs^+) complexes measured at the He buffer gas temperature (T_{BG}) of 86 K, which were converted from ATDs. All CCS distributions were fitted with two Gaussian functions with the width of the resolving power expected at T_{BG} = 86 K (Fig. 6, R = 45). These two bands were assigned to closed and open conformers by comparison between experimental and theoretical CCSs (Table 3). Figure 10 shows the most stable closed and open conformers of these complexes obtained by conformation search and quantum chemical calculations. As shown in Table 3, the relative intensity of the conformers depends on the encapsulated guest ion. In IM-MS, the relative intensity of the ion bands is directly related to the abundance ratio of the conformers. Regarding the abundance ratio of the closed conformers for these complexes, it is in such an order that $Ca^{2+} < Na^+ < Ag^+ < Cs^+ < Rb^+ < K^+$. The results imply that the ratio of the conformers is influenced by a combination of various factors, not proportional to one specific factor (for example, ionic diameter). The abundance ratio of the conformers is consistent with the relative Gibbs energies of conformers qualitatively. However, it is worth noting that the Gibbs energy is sensitive to the DFT functional. For example, the relative Gibbs energy at 86 K (ΔG_{86}) of the open conformer of K^+(DB24C8) is 1.2 kJ/mol in the DFT calculations at the M05-2X/6-311++G(d,p) level as shown in Table 3. However, at the ωB97X-D/6-311++G(d,p) level, the ΔG_{86} of the open conformer is 8.0 kJ/mol.

Figure 9d shows a CCS distribution of the K^+(DB24C8) complex at T_{BG} = 86 K. In the CCS distribution, two peaks were observed at 167.5 and 177.5 $Å^2$. In our previous study [22, 23], we computed the CCS distribution of K^+(DB24C8) based on the relative abundances and theoretical CCSs of the independent stable conformers without considering

Table 2 Ionic diameters of metal guest ions studied in the present study. Coordination number is 6 [41]

Ions	Ionic diameter / Å^2
Ca^{2+}	2.00
Na^+	2.04
Ag^+	2.30
K^+	2.76
Rb^+	3.04
Cs^+	3.34

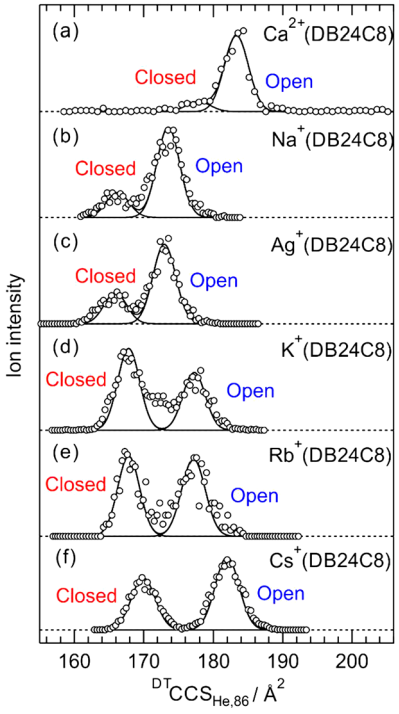

Figure 9 Observed CCS distribution of M(DB24C8) (M = Ca^{2+}, Na^+, Ag^+, K^+, Rb^+, Cs^+) by Cryo-IM-MS at 86 K

Table 3 Experimental CCSs and relative intensities of two bands in CCS distributions of M(DB24C8) (M = Ca^{2+}, Na^+, Ag^+, K^+, Rb^+, Cs^+) at T_{BG} = 86 K, and theoretical CCSs and relative Gibbs energies at T_{BG} = 86 K (ΔG_{86}) of the most stable closed and open conformers

Complex	Experiment		Theory		
	CCS / Å^2	Relative intensity	CCS / Å^2	Conformer	ΔG_{86} / kJ mol^{-1}
Ca^{2+}(DB24C8)	176.4 ± 0.7	0.12 ± 0.06	179.4 ± 1.1	Closed	10.6
	183.0 ± 0.2	1.0	183.9 ± 1.2	Open	0.0
Na^+(DB24C8)	164.4 ± 0.3	0.25 ± 0.06	161.0 ± 0.8	Closed	6.2
	172.0 ± 0.5	1.0	169.4 ± 0.7	Open	0.0
Ag^+(DB24C8)	165.2 ± 0.5	0.46 ± 0.08	162.8 ± 0.7	Closed	2.9
	172.9 ± 0.7	1.0	171.8 ± 0.9	Open	0.0
K^+(DB24C8)	167.5 ± 0.6	1.0	164.0 ± 0.7	Closed	0.0
	177.5 ± 0.7	0.70 ± 0.07	174.3 ± 1.0	Open	1.2
Rb^+(DB24C8)	167.8 ± 0.5	0.84 ± 0.10	165.7 ± 0.8	Closed	1.9
	177.0 ± 0.6	1.0	176.9 ± 0.9	Open	0.0
Cs^+(DB24C8)	169.6 ± 0.3	0.68 ± 0.16	166.5 ± 0.8	Closed	5.3
	181.9 ± 0.2	1.0	180.2 ± 0.9	Open	0.0

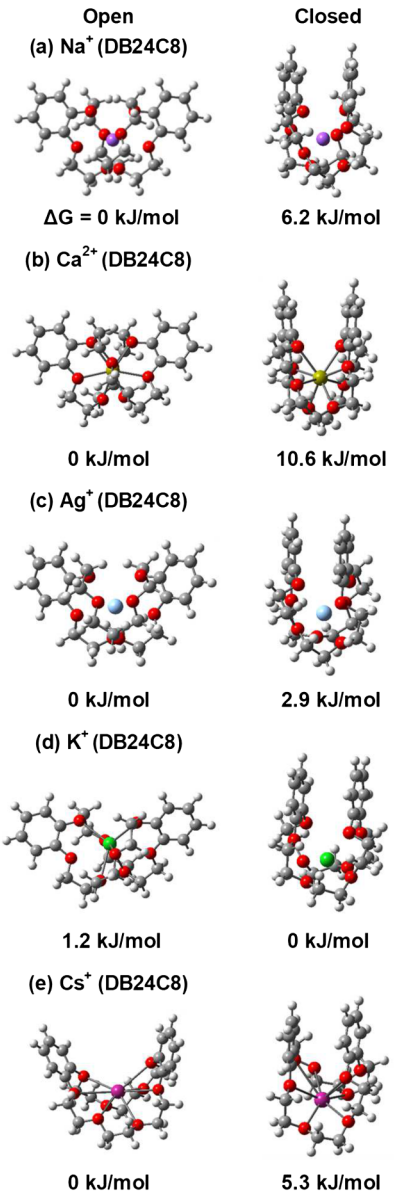

Figure 10 Most stable open and closed conformers of (**a**) Na^+(DB24C8), (**b**) Ca^{2+}(DB24C8), (**c**) Ag^+(DB24C8), (**d**) K^+(DB24C8), and (**e**) Cs^+(DB24C8). Relative Gibbs energies between the two conformers at $T_{BG} = 86$ K are also shown. Calculations were performed at the M05-2X/6-311++G(d,p) level with the modified effective core potential LanL2DZ for Ag atom, and Stuttgart RLC ECP for Cs atom

the isomerization of ions in the drift tube [simulation (1)]. By comparing experimental and computed CCS distributions, conformers with small and large CCSs were assigned to closed and open, respectively [21, 22]. In addition, the ion intensity between the closed and open bands was observed around 172 $Å^2$, while no ions appeared in the intermediate region in the computed CCS distribution. We concluded that the ion intensity around 172 $Å^2$ is caused by the isomerization reaction between the closed and open conformers in the drift tube which was also discussed in IM-MS at 300 K. In our previous paper [23], the activation energy of the isomerization reaction of K^+(DB24C8) was determined to be 5.9 ± 0.5 kJ mol^{-1} from the analysis of ATDs obtained by VT-Cryo-IM-MS. Details of the reaction mechanism were also discussed in our previous paper [23]. Similar isomerization reactions between the closed and open conformers were found to occur also for M(DB24C8) (M = Ag^+, Na^+, NH_4^+). The activation energies for these complexes were de-

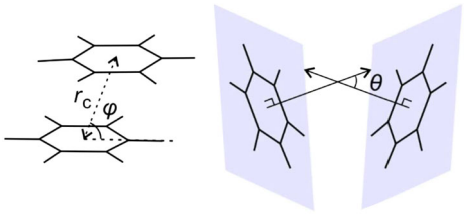

Figure 11 Parameters of benzene ring positional relationship (r_c: distance between benzene ring centers, θ: angle formed by normal vectors of two benzene planes, φ: angle between the benzene plane and the central line)

Table 4 Parameter values of benzene ring positional relationship in stable closed conformers for M(DB24C8) (M = Ca^{2+}, Na^+, Ag^+, K^+, Rb^+, Cs^+) and benzene dimer

Complex	r_c / Å	θ / deg	φ / deg
Ca^{2+}(DB24C8)	5.22	33.9	19.5, 18.8
Na^+(DB24C8)	4.88	15.3	33.2, 47.8
Ag^+(DB24C8)	4.91	19.4	32.0, 51.3
K^+(DB24C8)	3.83	0.1	63.2
Rb^+(DB24C8)	3.89	1.85	63.9
Cs^+(DB24C8)	4.15	13.8	64.6, 51.3
Benzene dimer [42]	3.85	0.0	65

termined to be 4.8–9.0 kJ mol^{-1} [23]. On the other hand, the ion intensity between closed and open bands was not observed in the CCS distribution of Cs^+(DB24C8) (Fig. 9f). This feature indicates the absence of isomerization reaction in Cs^+(DB24C8) at 86 K due to the high activation barrier between the two conformers.

To clarify the stability of the most stable closed conformer of K^+(DB24C8), the positional relationship between the two benzene rings of the complexes were extracted from the calculated structures. Three parameters (r_c, θ, φ) of the positional relationship were defined as shown in Fig. 11. The r_c is the distance between the benzene ring centers, θ is the angle formed by normal vectors of the two benzene planes, and φ is the angle between the benzene plane and the central line. Table 4 summarizes the optimized values of these parameters in M(DB24C8) (M = Ca^{2+}, Na^+, Ag^+, K^+, Rb^+, Cs^+) complexes. For comparison, the parameters of parallel-displaced conformers of a benzene dimer $(C_6H_6)_2$ obtained by ab initio calculation [42] are also shown in Table 4. As a result, the benzene ring positional relationship in K^+(DB24C8) was found to be quite close to that of the benzene dimer. Therefore, this closed conformer was concluded to show extraordinary stability because of the strong π-π interaction between the benzene rings due to its special benzene dimer-like conformation. For other complexes, the r_c is more distant and the θ is far from 0°, which may result in less contribution from the benzene-benzene π-π interaction. Meanwhile, it was also found that the stability of the closed conformer and thus the relative abundance are still more likely to be high when the r_c parameter of the two benzene rings on the conformer decreases and becomes closer to the benzene dimer. For example, after K^+ ion complex, Rb^+ ion complex is the second closest to the benzene dimer, and its abundance ratio was found to be higher in the actual Cryo-IM-MS observations. As mentioned above, the abundance ratio of the closed conformers to the open ones for six complexes is in the order, $Ca^{2+} < Na^+ < Ag^+ < Cs^+ < Rb^+ < K^+$. This order has a similar tendency with the descending order of r_c.

4 Conclusion

We applied variable-temperature cryogenic ion mobility-mass spectrometry (VT-Cryo-IM-MS) to the dibenzo-24-crown-8 (DB24C8) complexes with six metal ions (M = Ca^{2+}, Na^+, Ag^+, K^+, Rb^+, Cs^+) which are known as fundamental host-guest complexes. The two different types of conformers of K^+(DB24C8) were previously found by ultraviolet photodissociation spectroscopy under cold gas-phase conditions [38]. In the IM-MS at 300 K, the separation of the conformers of K^+(DB24C8) complex ions was impossible because the isomerization rate is much faster than the drift time (∼2 ms). We separated two types of conformers of M(DB24C8) complex ions by the Cryo-IM-MS at 86 K because the conformational change of the complex ions is suppressed in the cryogenic ion drift tube. These two conformers (closed and open) have different distances between two benzene rings of the DB24C8. The activation energy barrier of the isomerization reaction between the closed and open conformers of K^+(DB24C8) is lower than that of Cs^+(DB24C8). In the six M(DB24C8) complexes examined in this study, K^+(DB24C8) has the special stability of the closed conformer. This stability originates from the strong π-π interaction between two benzene rings of K^+(DB24C8). The present study reveals that the structural stability and flexibility of the host-guest complexes are dependent on the guest ion.

Acknowledgements
The authors acknowledge the support of the Research Center for Computational Science, Okazaki, Japan (Projects: 21-IMS-C054, 22-IMS-C054) with regard to providing computational resources.

Funding
The authors show gratefulness for supports from Japan Society for the Promotion of Science (KAKENHI, Grant Nos. JP16K05641, JP21H05418), The Institute for Quantum Chemical Exploration, and The Salt Science Research Foundation (Grant Nos. 1916, 2022, 2116).

Abbreviations
VT-Cryo-IM-MS, Variable-Temperature Cryogenic Ion Mobility-Mass Spectrometry; CCS, Collision Cross Section; DB24C8, Dibenzo-24-Crown-8; ESI, Electrospray Ionization; QIT, Quadrupole Ion Trap; TOF-MS, Time-of-Flight Mass Spectrometer; RF, Radio Frequency; PTFE, Poly(TetraFluoroEthylene); ATD, Arrival Time Distribution; DT-IMS, Drift-Tube type IMS.

Availability of data and materials
Data available upon request from the author.

Declarations

Competing interests
The authors declare no competing interests.

Author contributions
KO: Conceptualization, Validation, Writing – Original Draft. XH: Investigation, Analysis. RI: Investigation, Software, Analysis. KT: Investigation, Analysis. ST: Investigation, Analysis. FM: Writing—Review and Editing, Supervision. All authors read and approved the final manuscript.

Received: 12 January 2023 Accepted: 31 March 2023 Published online: 21 April 2023

References

1. Ebata T, Fujii M. Physical chemistry of cold gas-phase functional molecules and clusters. Singapore: Springer; 2019.
2. Lee S, Wyttenbach T, von Helden G, Bowers MT. Gas phase conformations of Li^+, Na^+, K^+, and Cs^+ complexed with 18-crown-6. J Am Chem Soc. 1995;117:10159–60.
3. Henderson SC, Valentine SJ, Counterman AE, Clemmer DE. ESI/ion trap/ion mobility/time-of-flight mass spectrometry for rapid and sensitive analysis of biomolecular mixtures. Anal Chem. 1999;71:291–301.
4. Bull JN, Scholz MS, Carrascosa E, da Silva G, Bieske EJ. Double molecular photoswitch driven by light and collisions. Phys Rev Lett. 2018;120:223002.
5. Seo J, Warnke S, Pagel K, Bowers MT, von Helden G. Infrared spectrum and structure of the homochiral serine octamer–dichloride complex. Nat Chem. 2017;9:1263–8.
6. Warnke S, Faleh AB, Toward RTR. High-throughput cryogenic IR fingerprinting of mobility-separated glycan isomers. ACS Meas Sci Au. 2021;1:157–64.

7. Zagorec-Marks W, Dodson LG, Weis P, Schneider EK, Kappes MM, Weber JM. Intrinsic structure and electronic spectrum of deprotonated biliverdin: cryogenic ion spectroscopy and ion mobility. J Am Chem Soc. 2021;143:17778–85.
8. Wyttenbach T, von Helden G, Batka Jr JJ, Carlat D, Bowers MT. Effect of the long-range potential on ion mobility measurements. J Am Soc Mass Spectrom. 1997;8:275–82.
9. Wyttenbach T, von Helden G, Bowers MT. Conformations of alkali ion cationized polyethers in the gas phase: polyethylene glycol and Bis[(Benzo-15-Crown-5)-15-Ylmethyl] pimelate. Int J Mass Spectrom Ion Process. 1997;165/166:377–90.
10. Milloy HB, Mass EMT. Discrimination in ion sampling from drift tubes. Int J Mass Spectrom Ion Phys. 1975;18:21–31.
11. Johnsen R, Chen A, Biondi A. Dissociative charge transfer of $\mathbf{He}^+$ ions with H_2 and D_2 molecules from 78 to 330 K. J Chem Phys. 1980;72:3085–8.
12. Koizumi T, Kobayashi N, Kaneko Y. Mobilities of $\mathbf{Ne}^+$ and $\mathbf{Ar}^+$ ions in He gas at 82 K. J Phys Soc Jpn. 1980;48:1678–82.
13. Misaizu F, Hori N, Tanaka H, Komatsu K, Furuya A, Ohno K. Isomer-selected photoreactions of gas-phase cluster ions. Eur Phys J D. 2009;52:59–62.
14. Wyttenbach T, Kemper PR, Bowers MT. Design of a new electrospray ion mobility mass spectrometer. Int J Mass Spectrom. 2001;212:13–23.
15. May JC, Russell DH. A mass-selective variable-temperature drift tube ion mobility-mass spectrometer for temperature dependent ion mobility studies. J Am Soc Mass Spectrom. 2011;22:1134–45.
16. Servage KA, Silveira JA, Fort KL, Russell DH. Cryogenic ion mobility-mass spectrometry: tracking ion structure from solution to the gas phase. Acc Chem Res. 2016;49:1421–8.
17. Ujma J, Giles K, Morris M, Barran PE. New high resolution ion mobility mass spectrometer capable of measurements of collision cross sections from 150 to 520 K. Anal Chem. 2016;88:9469–78.
18. von Helden G, Wyttenbach T, Bowers MT. Inclusion of a MALDI ion source in the ion chromatography technique: conformational information on polymer and biomolecular ions. Int J Mass Spectrom Ion Process. 1995;146/147:349–64.
19. Gidden J, Bowers MT. Gas-phase conformational and energetic properties of deprotonated dinucleotides. Eur Phys J D. 2002;20:409–19.
20. Weis P, Bierweiler T, Vollmer E, Kappes MM. $\mathbf{Au}_9^+$: rapid isomerization reactions at 140 K. J Chem Phys. 2002;117:9293–7.
21. Tainaka S, Ujihira T, Kubo M, Kida M, Shimoyama D, Muramatsu S, Abe M, Haino T, Ebata T, Misaizu F, Ohshimo K, Inokuchi Y. Conformation of K^+ (crown ether) complexes revealed by ion mobility-mass spectrometry and ultraviolet spectroscopy. J Phys Chem A. 2020;124:9980–90.
22. Ohshimo K, He X, Ito R, Misaizu F. Conformer separation of dibenzo-crown-ether complexes with Na^+ and K^+ ions studied by cryogenic ion mobility-mass spectrometry. J Phys Chem A. 2021;125:3718–25.
23. Ito R, Ohshimo K, Misaizu F. Structures of dibenzo-24-crown-8 complex with an $\mathbf{NH}_4^+$ ion studied by cryogenic ion mobility-mass spectrometry. Chem Phys Lett. 2022;794:139510.
24. Ito R, He X, Ohshimo K, Misaizu F. Large conformational change in the isomerization of flexible crown ether observed at low temperature. J Phys Chem A. 2022;126:4359–66.
25. Ohshimo K, Sato R, Misaizu F. Intramolecular dispersion attraction in tetraalkylammonium cations revealed by cryogenic ion mobility mass spectrometry. J Phys Chem A. 2020;124:7999–8004.
26. Norgate EL, Upton R, Hansen K, Bellina B, Brookes C, Politis A, Barran PE. Cold denaturation of proteins in the absence of solvent: implications for protein storage. Angew Chem, Int Ed Engl. 2022;61:e202115047.
27. Poyer S, Comby-Zerbino C, Choi CM, MacAleese L, Deo C, Bogliotti N, Xie J, Salpin JY, Dugourd P, Chirot F. Conformational dynamics in ion mobility data. Anal Chem. 2017;89:4230–7.
28. Kelly RT, Tolmachev AV, Page JS, Tang K, Smith RD. The ion funnel: theory, implementations, and applications. Mass Spectrom Rev. 2010;29:294–312.
29. Jones RM, Anderson SL. Simplified radio-frequency generator for driving ion guides, traps, and other capacitive loads. Rev Sci Instrum. 2000;71:4335–7.
30. Revercomb HE, Mason EA. Theory of plasma chromatography / gaseous electrophoresis—a review. Anal Chem. 1975;47:970–83.
31. Gabelica V, Shvartsburg AA, Afonso C, Barran P, Benesch JLP, Bleiholder C, Bowers MT, Bilbao A, Bush MF, Campbell JL, Campuzano IDG, Causon T, Clowers BH, Creaser CS, Pauw ED, Far J, Fernandez-Lima F, Fjeldsted JC, Giles K, Groessl M, Hogan Jr CJ, Hann S, Kim HI, Kurulugama RT, May JC, McLean JA, Pagel K, Richardson K, Ridgeway ME, Rosu F, Sobott F, Thalassinos K, Valentine SJ, Wyttenbach T. Recommendations for reporting ion mobility mass spectrometry measurements. Mass Spectrom Rev. 2019;38:291–320.
32. Aoyagi S, Nishibori E, Sawa H, Sugimoto K, Takata M, Miyata Y, Kitaura R, Shinohara H, Okada H, Sakai T, Ono Y, Kawachi K, Yokoo K, Ono S, Omote K, Kasama Y, Ishikawa S, Komuro T, Tobita H. A layered ionic crystal of polar $Li@C_{60}$ superatoms. Nat Chem. 2010;2:678–83.
33. Matsuo Y, Okada H, Ueno H. Endohedral lithium-containing fullerenes preparation, derivatization, and application. Singapore: Springer; 2017.
34. Okada H, Anion MY. Exchange of $Li^+@C_{60}$ salt for improved solubility. Fuller Nanotub Carbon Nanostruct. 2014;1(3):262–8.
35. Mesleh MF, Hunter JM, Shvartsburg AA, Schatz GC, Jarrold MF. Structural information from ion mobility measurements: effects of the long-range potential. J Phys Chem. 1996;100:16082–6.
36. Frisch MJ, Trucks GW, Schlegel HB, Scuseria GE, Robb MA, Cheeseman JR, Scalmani G, Barone V, Petersson GA, Nakatsuji H et al. Gaussian 16, revision C.01. Wallingford: Gaussian Inc.; 2019.
37. Campuzano I, Bush MF, Robinson CV, Beaumont C, Richardson K, Kim H, Kim HI. Structural characterization of drug-like compounds by ion mobility mass spectrometry: comparison of theoretical and experimentally derived nitrogen collision cross sections. Anal Chem. 2012;84:1026–33.
38. Kida M, Kubo M, Ujihira T, Ebata T, Abe M, Inokuchi Y. Selective probing of potassium ion in solution by intramolecular excimer fluorescence of dibenzo-crown ethers. ChemPhysChem. 2018;19:1331–5.
39. Goto H, Osawa E. Corner flapping: a simple and fast algorithm for exhaustive generation of ring conformations. J Am Chem Soc. 1989;111:8950–1.

40. Goto H, Osawa E. An efficient algorithm for searching low-energy conformers of cyclic and acyclic molecules. J Chem Soc, Perkin Trans. 1993;2(2):187–98.
41. Shannon RD. Revised effective ionic radii and systematic studies of interatomic distances in halides and chalcogenides. Acta Crystallogr. 1976;A32:751–67.
42. Hobza P, Selzle HL, Schlag EW. New structure for the most stable isomer of the benzene dimer: a quantum chemical study. J Phys Chem. 1993;97:3937–8.

Publisher's Note